3

Unified Design of Wireless Information and Power Transmission

Dong In Kim[*]*, Jong Jin Park, Jong Ho Moon, and Kang Yoon Lee*

School of Information and Communication Engineering, Sungkyunkwan University (SKKU), Korea

3.1 Introduction

With the growing interest in the Internet-of-Things (IoT), massive connection of low-power IoT/wearable devices is desired for machine-type communication (MTC), and battery lifetime is becoming a crucial issue for operating IoT networks perpetually [1, 2]. Hence, a fundamental paradigm shift should be launched to develop low-power transceivers, such as ambient backscatters [3] and LoRa backscatters using chirp spread spectrum (CSS) [4], enabling the vision of low-power smart devices with ubiquitous connectivity. Furthermore, smart devices may need to be self-powered for energy neutral operation. Self-powered smart devices, charged by ambient renewable resources instead of requiring battery replacement, can be deployed to enable low-power wide area networks (LP-WAN) for IoT [5]. One promising solution is simultaneous wireless information and power transfer (SWIPT), a technique that transfers both information and power in the air using a radio frequency (RF) signal. Existing SWIPT approaches aim to enhance the rate–energy tradeoff [6, 7] through optimum waveform design for SWIPT on the one hand, and via implementation of appropriate receiver structures on the other hand, at both circuit and system levels.

SWIPT uses a single tone (carrier) with amplitude and/or phase modulation for low-complexity devices. Recently, it was shown that using multi-tone waveforms can boost up the efficiency of wireless power transfer (WPT) due to the nonlinear rectification process [8, 9], but a simple modulation based on a single tone cannot be used with multi-tone waveforms. To tackle this difficulty, we have proposed peak-to-average power ratio (PAPR) based SWIPT [10], a

---

[*]Corresponding author: Dong In Kim; dikim@skku.ac.kr

technique that uses multi-tone waveforms for energy transfer and their distinct levels of PAPR to convey information. Multi-tone (PAPR) based SWIPT yields higher WPT efficiency with increased operational range and low-power information decoding, but it suffers from a lower rate than single tone based SWIPT. Therefore, we should optimize the tradeoff between achievable rate and harvested energy as well as the operational range.

To empower the LP-WAN with ubiquitous connectivity for IoT, the operational range of self-powered smart devices needs to be enlarged, which depends largely on the end-to-end efficiency of WPT. In this chapter, we reveal that the efficiency in fact varies with both the RF input power at the rectifier and the specific RF signal waveform being used for SWIPT, which has motivated us to implement dual mode SWIPT. For this, we propose a new transceiver architecture for SWIPT with adaptive mode switching (MS) between single and multi-tone waveforms via an adaptive power management and information decoding (PM-&-ID) module to control the operational range for energy neutral operation. Furthermore, the WPT efficiency relies on the circuit design of the rectifier because of the nonlinear rectification process, and we propose a reconfigurable energy harvester with multiple energy harvesting (EH) circuits implemented in parallel before the battery.

The rest of this chapter is organized as follows. In Section 3.2 we present nonlinear EH models along with the measured RF-to-direct current (DC) power conversion efficiency (PCE), which provides useful insights for designing dual mode SWIPT. Section 3.3 proposes a new waveform and transceiver design for multi-tone (PAPR) based SWIPT with higher WPT efficiency and dual mode SWIPT for an increased operational range. In Section 3.4 we further propose the reconfigurable energy harvester for enlarging the linear region of the PCE over wide input power ranges.

Notations. The main notations used in this chapter are summarized in Table 3.1. We use boldface lower case letters to denote vectors. $(\cdot)^*$ represents the complex conjugate; $|\cdot|$ and $\|\cdot\|$ denote the absolute value of a complex scalar and the l_2-norm of a vector, respectively; the normal distribution is denoted by $\mathcal{N}(\mu, \sigma^2)$ with mean μ and variance σ^2; $\sim$ stands for "distributed as"; **Re** and **E** denote the real parts of a complex number and expectation, respectively; $\Pr[X]$ represents the probability of event X.

3.2 Nonlinear EH Models

We consider a SWIPT system which uses single/multi-tone waveforms for signaling and is equipped with $K \geq 1$ transmit antennas and a single receive antenna. Most previous studies on SWIPT systems assumed an ideal linear energy harvester [11]–[13], in which the RF-to-DC PCE ζ is modeled as a fixed

Table 3.1 Nomenclature adopted in this chapter

Notation	Description
P_T/P_R	Transmit/receive power
P_{in}	Input power of EH circuit
P_{EH} ($P_{EH,x}$)	EH power ($x = L, NL$ for linear/nonlinear)
P_{sat}	Maximum EH power due to diode saturation
P_{th}	Input power threshold for dual mode operation
P_C	Circuit power consumption of the receiver
ζ	Power conversion efficiency (PCE)
R	Achievable data rate
B_T/B_C	Transmit/coherence bandwidth
W	Signal bandwidth
$Q(N)$	Number of total (selected) multi-tone waveforms
f_c	Carrier frequency
Δf	Minimum spacing of multi-tone waveforms
h	Complex-valued channel gain
$\eta(t)$	Noise signal
N_o	Noise power spectral density level
$T(T_x)$	Symbol time ($x = s, m$ for single/multi-tone)
K	Number of array antennas
M	Modulation index
ρ	Power-splitting ratio
p_{out}	Outage probability
p_b	Bit-error rate (BER)
p_{tag}	Target BER
N_{EH}	Number of EH circuits
α	Receive mode indicator variable
B	Number of fading blocks

constant independent of the input power P_{in}. Under the linear EH model, the harvested power can be described as $P_{EH,L} = \zeta P_{in}$ ($0 \leq \zeta \leq 1$). However, considering the nonlinear rectification process (diode turn-on/reverse breakdown voltages, diode nonlinearity, and saturation effects reported in [8, 9, 14]), the harvested power P_{EH} cannot be simply predicted by the conventional linear model. In fact, the PCE of the EH circuit is generally a function of the input signal waveform (e.g., both the amplitude and phase in the case of a sinewave). Thus, the PCE is a function of not only the input power (e.g., the squared amplitude of the sinewave), but also the shape of the input signal (e.g., the phase of the sinewave).

To address the nonlinear characteristics and to improve accuracy, new non-linear EH models were proposed in [9], [14]. On the one hand, the nonlinear EH model in [9] shows that for the single diode rectifier circuit, the output DC current of the diode (i.e., the output DC power of the rectifier for a given load resistance) with the fourth-order Taylor series truncation is given by

$$i_{out} = c_2 \mathbf{E}\left[y^2(t)\right] + c_4 \mathbf{E}\left[y^4(t)\right] \tag{3.1}$$

where $c_j = \frac{i_s}{j! n_f^j v_t^j} (\sqrt{R_{ant}})^j$ for $j = 2, 4$, i_s, n_f, v_t, and R_{ant} are the reverse bias saturation current, the ideality factor, the thermal voltage of the diode, and the resistance of the receive antenna, respectively. Also, in (3.1), $y(t)$ denotes the received RF signal, which is given by

$$y(t) = \mathbf{Re}\left[\sum_{n=1}^{N} h_n s_n e^{j(2\pi f_n t + \phi_n)}\right]. \tag{3.2}$$

Here, h_n, f_n, s_n, and ϕ_n denote the complex channel, the carrier frequency, the amplitude, and the phase for the nth sinewave. As can be seen from (3.1) and (3.2), the PCE is a function of the input signal waveform (i.e., s_n and ϕ_n values) because the output DC current i_{out} is a function of the received RF signal $y(t)$, which is actually a function of the input power and the shape of the input signal.

However, the nonlinear model of (3.1) is valid only for a small signal, resulting in huge inaccuracy outside the small-signal range. On the other hand, a nonlinear EH model based on logistic function was suggested in [14], where the fitted harvested power $P_{EH,NL}$ is expressed as

$$P_{EH,NL} = \frac{P_{sat}(1 - e^{-c_1 P_{in}})}{1 + e^{-c_1(P_{in} - c_0)}}. \tag{3.3}$$

Here, c_0 and c_1 are constants related to the EH circuit specification and the shape of the input signal. Given the EH circuit and input signal, we can obtain P_{sat}, c_0, and c_1 using a curve-fitting tool. Specifically, the nonlinear model of (3.3) tackles the nonlinearity of the PCE of the rectifier (including the turn-on and saturation nonlinearities) and it characterizes the nonlinearity in terms of the input power, whereas the model of (3.1) tackles the diode nonlinearity due to the nonlinear diode characteristic and it characterizes the nonlinearity in terms of the input signal waveform. However, the nonlinear model of (3.3) may be inaccurate in the low power region for wide input power ranges.

Figure 3.1 shows the *measured* RF-to-DC PCE of the single diode rectifier circuit over a wide input power range (-20–15 dBm) when single/multi-tone waveforms ($N = 1, 2, 4, 8, 16$) are used with a single transmit antenna ($K = 1$). For a given shape (i.e., fixed N) of the input signal, the PCE depends mainly on the input power (i.e., P_{in}). In this case, the PCE typically increases with the input power, and then remains nearly constant where the input power exceeds a
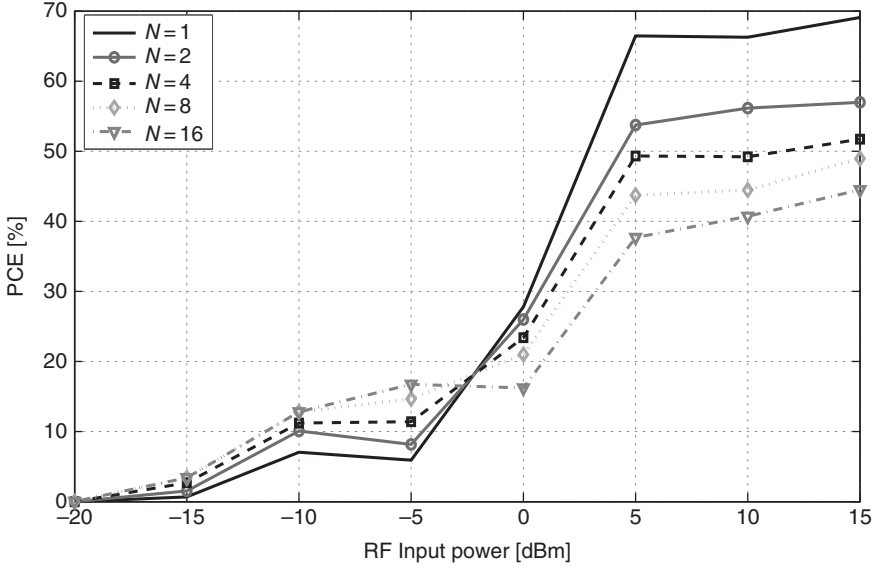
Figure 3.1 Measured RF-to-DC power conversion efficiency (PCE) of the single diode rectifier circuit for both single tone ($N = 1$) and multi-tone waveforms ($N = 2, 4, 8, 16$).

certain threshold. On the other hand, for a given input power the PCE depends mainly on the shape of the input signal (i.e., N).

Therefore, we may consider adaptive MS between single and multi-tone waveforms to achieve the maximum PCE. For this, we define the input power threshold P_{th} for adaptive MS, which depends only on the circuit specification. For example, P_{th} is -3 dBm for the single-stage rectifier in Figure 3.1.

3.3 Waveform and Transceiver Design

3.3.1 Multi-tone (PAPR) based SWIPT

Multi-tone Waveforms and Transmit/Receive PAPR. A new transceiver architecture for SWIPT using multi-tone waveforms and their distinct PAPR is shown in Figure 3.2. First, the information is encoded by selecting a subset of the multi-tone waveforms having a specific level of PAPR as follows. Suppose there are Q tones available for SWIPT with minimum spacing Δf, such that

$$\mathcal{F} = \{f_1, f_2, \dots, f_Q\} \tag{3.4}$$

where $f_i = f_1 + (i - 1)\Delta f$ for $i = 1, \dots, Q$. The subset $\mathcal{F}_N \subset \mathcal{F}$ is defined as

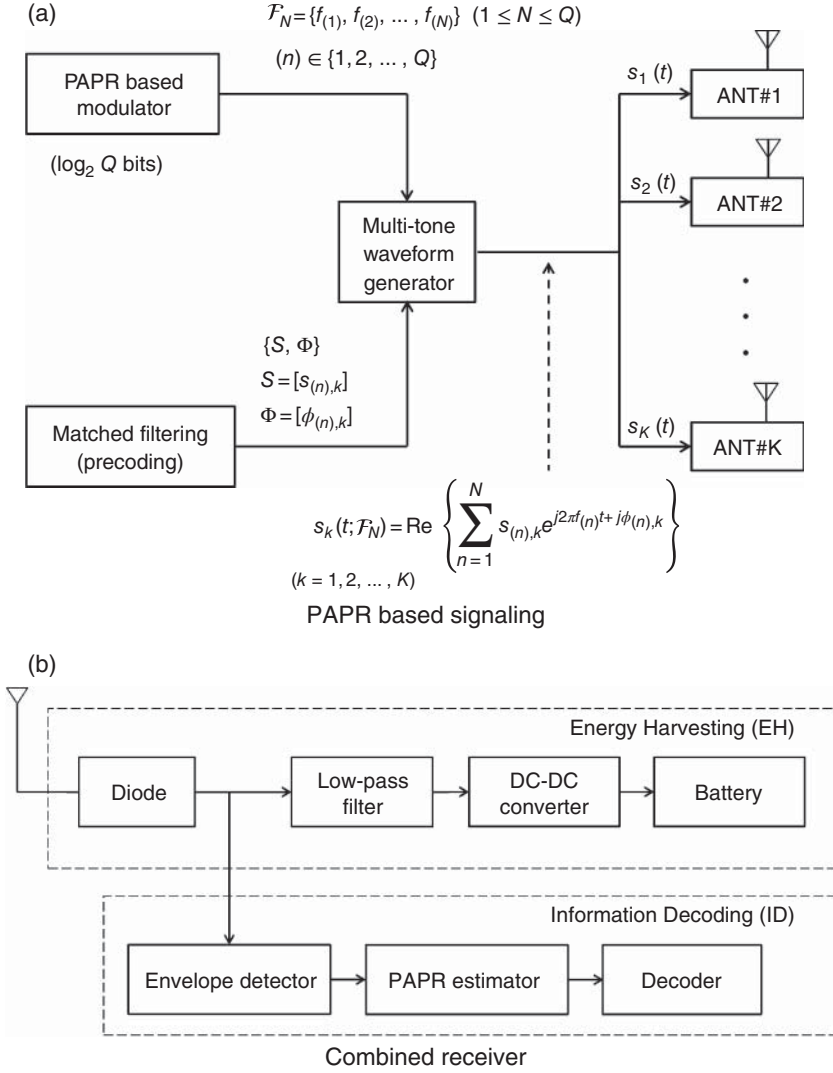$$\mathcal{F}_N = \{f_{(1)}, f_{(2)}, \dots, f_{(N)}\} \tag{3.5}$$

(a)

$\mathcal{F}_N = \{f_{(1)}, f_{(2)}, \ldots, f_{(N)}\}$ $(1 \le N \le Q)$

$(n) \in \{1, 2, \ldots, Q\}$

PAPR based modulator

$(\log_2 Q$ bits$)$

Multi-tone waveform generator

$\{S, \Phi\}$
$S = [s_{(n),k}]$
$\Phi = [\phi_{(n),k}]$

Matched filtering (precoding)

$s_1(t)$ → ANT#1

$s_2(t)$ → ANT#2

$s_K(t)$ → ANT#K

$$s_k(t; \mathcal{F}_N) = \mathrm{Re} \left\{ \sum_{n=1}^{N} s_{(n),k} e^{j2\pi f_{(n)}t + j\phi_{(n),k}} \right\}$$

$(k = 1, 2, \ldots, K)$

PAPR based signaling

(b)

Energy Harvesting (EH)

Diode → Low-pass filter → DC-DC converter → Battery

Information Decoding (ID)

Envelope detector → PAPR estimator → Decoder

Combined receiver

Figure 3.2 A new transceiver architecture for SWIPT using multi-tone waveforms for energy transfer and their distinct PAPR for information transmission. In the combined receiver (b), the time constant for envelope detection is shorter than that for low-pass filtering to yield the DC output.

Table 3.2 An example mapping when $Q = 4$

2 bits	N	$PAPR_{TX}$	$\mathcal{F}_N$
[00]	1	2	$\{f_{(1)}\}$
[01]	2	4	$\{f_{(1)}, f_{(2)}\}$
[10]	3	6	$\{f_{(1)}, f_{(2)}, f_{(3)}\}$
[11]	4	8	$\{f_1, f_2, f_3, f_4\}$

where $(n) \in \{1, 2, \ldots, Q\}$ for $1 \le n \le N$ and $(n) \ne (n')$ if $n \ne n'$. The $\log_2 Q$-bit information can be one-to-one mapped to $\mathcal{F}_N$ in an increasing order of $N = |\mathcal{F}_N| = 1, \ldots, Q$, as illustrated in Table 3.2. Note that all distinct subsets of same size N produce the same level of PAPR in (3.8) below, and $\mathcal{F}_N$ acts as the *best* subset whose N tones experience relatively better channel gains, especially for the frequency-selective (FS) channel.[1] Assume that an array of K antennas is used at the transmitter for enhancing WPT efficiency. Then, the multi-tone waveforms for the kth antenna, which are generated by subset $\mathcal{F}_N$, can be expressed as

$$s_k(t; \mathcal{F}_N) = \mathbf{Re} \left\{ \sum_{n=1}^{N} s_{(n),k} \exp[\, j2\pi f_{(n)} t + j\phi_{(n),k} \,] \right\} \tag{3.6}$$

for $k = 1, \ldots, K$. Here, $s_{(n),k}$ and $\phi_{(n),k}$ are the magnitude and initial phase associated with the (n)th tone $f_{(n)}$ at the kth antenna. Note that a total transmit power of P_T is shared by the K antennas, subject to

$$\sum_{k=1}^{K} \mathbf{E} \left\{ |s_k(t; \mathcal{F}_N)|^2 \right\} \le P_T. \tag{3.7}$$

Now, the $\log_2 Q$-bit information is conveyed via the distinct PAPR of $s_k(t; \mathcal{F}_N)$ ($k = 1, \ldots, K$) through the subset $\mathcal{F}_N$, which can be evaluated as

$$PAPR_{TX}^k(N) = \frac{\max_{t \in [0,T]} |s_k(t; \mathcal{F}_N)|^2}{\frac{1}{T} \int_T |s_k(t; \mathcal{F}_N)|^2 dt} \le 2N. \tag{3.8}$$

Here, the upper bound on the *transmit* PAPR, namely $PAPR_{TX} = 2N$, can be achieved with uniform power allocation among N tones and K antennas and all initial phases aligned, such that

$$s_{(n),k} = \sqrt{\frac{2P_T}{NK}} \quad \text{and} \quad \phi_{(n),k} = \phi \quad \text{for } \forall\ n, k. \tag{3.9}$$

---

1 This implies that knowledge of the channel state information (CSI) will allow selection of the *best* subset $\mathcal{F}_N$ of N tones in a given transmission time.

Thus, it is necessary to perform the matched-filtering (MF) through the channel to achieve amplitude matching and phase alignment at the receiver.

Given an array of K antennas is used for SWIPT, the received signal can be expressed as

$$r(t; \mathcal{F}_N) = \mathbf{Re} \left\{ \sum_{k=1}^{K} \sum_{n=1}^{N} s_{(n),k} h_{(n),k} \exp[\, j2\pi f_{(n)} t + j\phi_{(n),k} \,] \right\} + \eta(t), \quad (3.10)$$

where the noise $\eta(t)$ is zero mean with variance $\sigma^2 = N_o W$. Here, N tones in $\mathcal{F}_N$ are assumed to be spaced over a *selective* sub-band of the coherence bandwidth B_c (i.e., W), which gives similar Rayleigh-faded channel gains for different tones but independent channel gains for different antennas. The composite channel gains $\{h_{(n),k}\}$ are assumed to be estimated by sending a short pilot signal to the transmitter before each frame transmission, assuming the channel reciprocity holds for SWIPT.

To achieve a high WPT efficiency and also the upper bound of the transmit PAPR, we assume that the transmitter performs the MF precoding for the amplitude matching and phase alignment at the receiver. Therefore, the complex envelope of the (n)th tone in the multi-tone waveforms for the kth antenna should be adjusted as

$$s_{(n),k} \exp(j\phi_{(n),k}) = \sqrt{2P_T} \frac{h_{(n),k}^*}{\sqrt{\sum_{k=1}^{K} \sum_{n=1}^{N} |h_{(n),k}|^2}}, \quad (3.11)$$

where the transmit power constraint in (3.7) has been applied. Using the channel vector $\mathbf{h}_{(n)} = [h_{(n),1}, h_{(n),2}, \ldots, h_{(n),K}]$, the received signal in (3.10) after the precoding can be simplified to

$$r(t; \mathcal{F}_N) = \sqrt{\frac{2P_T}{\sum_{n=1}^{N} \| \mathbf{h}_{(n)} \|^2}} \sum_{n=1}^{N} \| \mathbf{h}_{(n)} \|^2 \cos(2\pi f_{(n)} t) + \eta(t). \quad (3.12)$$

At the receiver, the rectifier in Figure 3.2b performs the RF-to-DC conversion and follows the envelope of the received signal in (3.12), based upon which the *receive* PAPR is measured as

$$PAPR_{RX}(N) = \frac{\max_{t \in [0,T]} |r(t; \mathcal{F}_N)|^2}{\frac{1}{T} \int_T |r(t; \mathcal{F}_N)|^2 dt} \cong \frac{\left| \sqrt{2P_T \sum_{n=1}^{N} \| \mathbf{h}_{(n)} \|^2} + \eta \right|^2}{\frac{P_T \sum_{n=1}^{N} \|\mathbf{h}_{(n)}\|^4}{\sum_{n=1}^{N} \|\mathbf{h}_{(n)}\|^2} + N_o B_c}. \quad (3.13)$$

If the noise can be ignored, given the received power level is -10 dBm for energy signals, unlike the -60 dBm for information signals, the receive PAPR reduces to

$$PAPR_{RX}(N) \cong \frac{2 \left(\sum_{n=1}^{N} \| \mathbf{h}_{(n)} \|^2 \right)^2}{\sum_{n=1}^{N} \| \mathbf{h}_{(n)} \|^4}. \quad (3.14)$$

Moreover, if the channel appears frequency flat (FF), namely $\mathbf{h}_{(n)} = \mathbf{h}$ for $\forall n$, then the receive PAPR achieves the upper bound as

$$PAPR_{RX}(N) \cong \frac{2N \parallel \mathbf{h} \parallel^4}{\parallel \mathbf{h} \parallel^4} = 2N. \tag{3.15}$$

Remarks. It is interesting to see that the receive PAPR can achieve the upper bound $PAPR_{RX} = PAPR_{TX} = 2N$ regardless of the channel vector $\mathbf{h}_{(n)}$, which implies that the WPT can be maximized with the MF precoding at the transmitter, while achieving the upper bound on the transmit PAPR at the receiver. *In particular, the channel estimation is not required at the receiver for the PAPR based information decoding in an FF channel.* Even if the channel appears FS, we can identify a sub-band with high channel gain where the channel appears FF, thereby avoiding channel estimation.

Evaluation. To validate the PAPR based information transmission, the bit-error rate (BER) performance is evaluated as

$$p_b(N) = 1 - \Pr\left[2N - 1 \le PAPR_{RX}(N) < 2N + 1\right] \tag{3.16}$$

for $2 \le N \le Q - 1$ and

$$p_b(N) = \begin{cases} \Pr\left[PAPR_{RX}(N) \ge 3\right] & \text{for } N = 1, \\ 1 - \Pr\left[PAPR_{RX}(N) \ge 2Q - 1\right] & \text{for } N = Q. \end{cases} \tag{3.17}$$

Figure 3.3 shows the BER performance versus the average received SNR when $K = 1$ for both FF ($B_T = 1$ MHz) and FS ($B_T = 10$ MHz) channels. In the FS channel, we select a sub-band of $B_c = 1$ MHz where the channel appears FF. Here, the numerical BER evaluations based on (3.13), (3.16) and (3.17) are validated by Monte Carlo simulations. Furthermore, the BER performance of PAPR based signaling ($Q = 16$) is compared with that of single tone signaling with $M = 16$-ary PAM. We observe that their BER performance is comparable in the SNR range of interest.

The multi-tone waveforms for SWIPT are generated with the minimum spacing $\Delta f = T^{-1}$. Hence, if we define $B_c \ll B_T$ as a sub-band with higher channel gain for the FS channel, the information rate can be evaluated as

$$R_b = \frac{1}{T} \log_2(1 + B_c T) \quad \text{bits/s} \tag{3.18}$$

for $Q = 1 + B_c T$. We observe that as Q increases, the harvested power offered by multi-tone waveforms is increased, referring to [9]

$$\text{DC output} = \frac{1}{Q} \sum_{N=1}^{Q} \left(c_2 P_R + 2c_4 \frac{2N^2 + 1}{2N} P_R^2 \right) \tag{3.19}$$

when $K = 1$. However, T in (3.18) is also increased with fixed B_c, resulting in reduced R_b. Hence, there exists a rate-energy tradeoff for varying Q by which
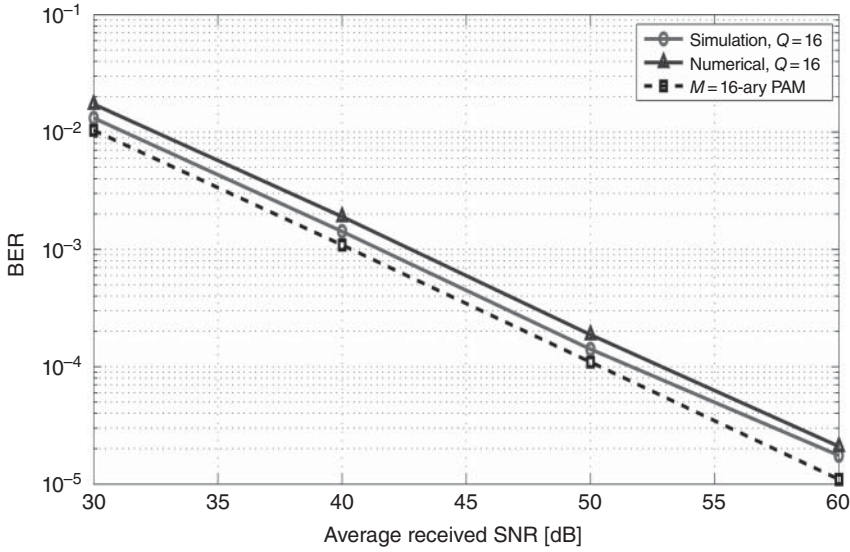
Figure 3.3 BER versus average received SNR for PAPR based signaling with $Q = 16$ tones and single tone signaling with $M = 16$-ary pulse amplitude modulation (PAM).

B_c can be properly selected, considering a specific channel gain offered by a sub-band within B_T in the FS channel.

In Figure 3.4, the DC output is normalized to one for a single tone ($Q = 1$), where the achievable data rate increases with increased $M = 2, 4, 8, 16, 32, 64$, subject to the target BER of 10^{-3}. Note that the data rate of the single tone with M-ary PAM is set to $R_{PAM} = B_c \log_2 M$ for $B_c = 1$ MHz, subject to the target BER for all M above. This is true when the energy signal yields the received SNR above 50 dB at the received power $P_R = -20$ dBm with the noise level of typically -130 dBm/Hz over the sub-band of 1 MHz. The proposed SWIPT using multi-tone waveforms with $Q = 2, 4, 8, 16, 32, 64$ produces much higher normalized DC output in (3.19), relative to the single tone ($Q = 1$), though the data rate in (3.18) decreases with increased Q. For low-rate IoT sensors, the operational range of RF energy transfer to a sensor node is most critical and can be greatly enlarged with multi-tone (PAPR) SWIPT.

3.3.2 Dual Mode SWIPT

Waveform Design and Transmitter Architecture. For dual mode SWIPT, an integrated transmitter generates two types of single and multi-tone waveforms, as shown in Figure 3.5. The transmitter selects a waveform according to the adaptive MS policy, which depends on the received power at the receiver.
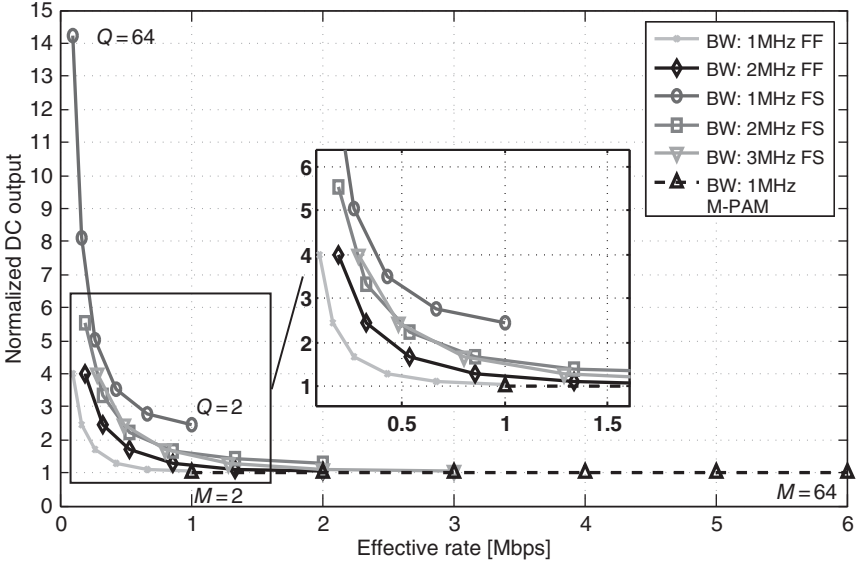
Figure 3.4 Rate–energy tradeoff for varying Q and M in multi-tone waveforms with PAPR and single tone waveform with M-ary PAM, respectively.

Single tone/multilevel PSK. The single tone waveform is optimized for high data rate, unlike the multi-tone waveforms. We consider single tone signaling of multiple energy levels and phase-shift keying (PSK) as

$$s_s(t) = \mathbf{Re} \{A \exp(j2\pi f_c t + j\theta)\}, \tag{3.20}$$

where $A \in \{d\sqrt{2}, 2d\sqrt{2}, ..., N_e d\sqrt{2}\}$ and $\theta \in \{\frac{2\pi}{N_p}, 2\frac{2\pi}{N_p}, ..., 2\pi\}$ are the amplitude and phase of the modulated symbol, and f_c is the center frequency of the signal. N_e denotes the number of energy levels (e.g., the inner/outer circles in Figure 3.5), where d is the constellation unit distance, and N_p is the number of signal (phase) points per level. The unit distance d can be obtained from the average signal power relationship as

$$P_T = \frac{N_p \sum_{n=1}^{N_e} (nd)^2}{M}, \tag{3.21}$$

where $M = N_e N_p$. The energy-level/phase information is decoded jointly at the receiver.

Multi-tone/PAPR modulation. As the distance from the access point (AP) is increased, the transmit power should be increased to compensate for the severe propagation loss. We may enhance the efficiency of WPT by using multi-tone waveforms, which effectively increases the operational range, thanks to the nonlinear rectification process. Furthermore, the PAPR based
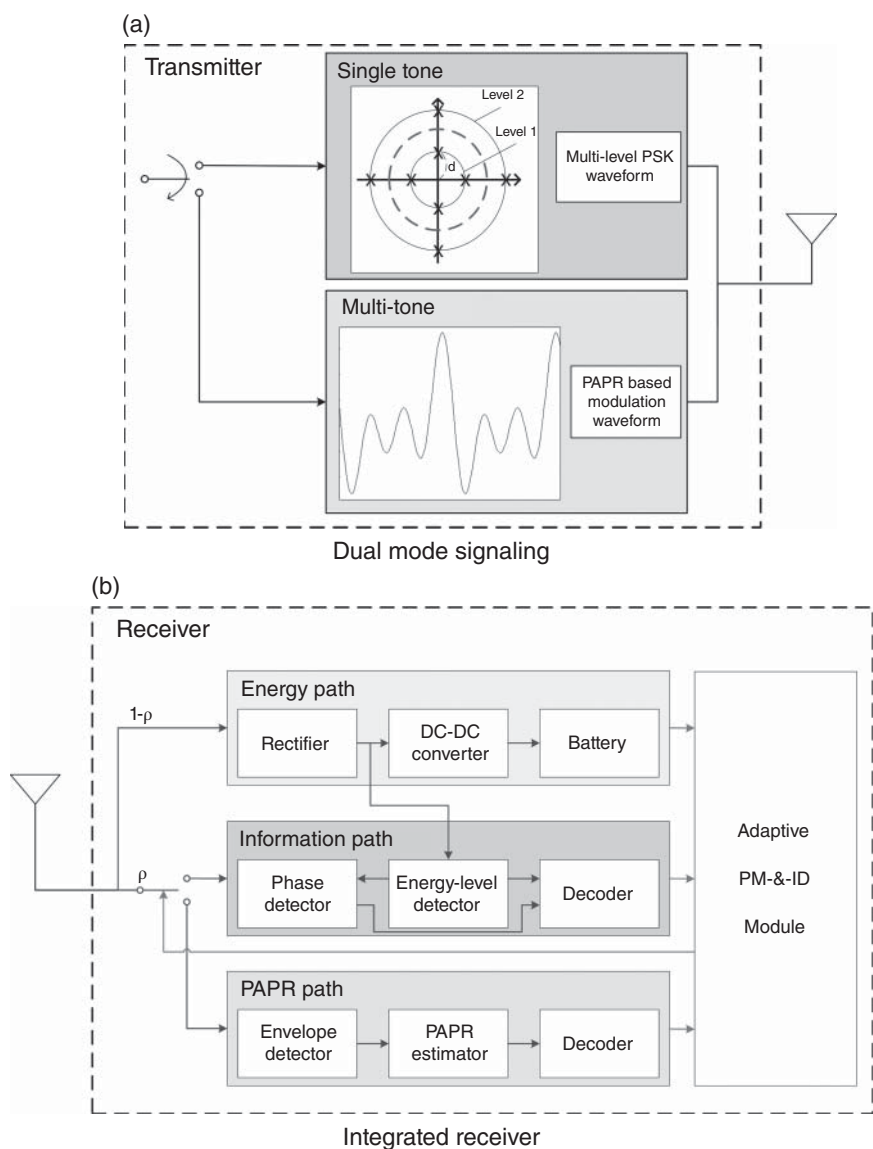
(a)

Dual mode signaling

(b)

Integrated receiver

Figure 3.5 A new transceiver architecture for dual mode SWIPT.

information transmission facilitates low-power decoding via simple PAPR measurements [10]. For the maximum transmit PAPR with a single antenna $K = 1$ in (3.9), the PAPR modulated signal using a subset of N tones from Q available tones (i.e., $N \in \{1, ..., Q\}$) is given by

$$s_m(t) = \mathbf{Re} \left\{ \sum_{n=1}^{N} \sqrt{\frac{2P_T}{N}} \exp[\, j2\pi f_{(n)}t + j\phi\,] \right\}. \tag{3.22}$$

To achieve a high WPT efficiency, we assume that the transmitter performs the MF precoding for amplitude matching and phase alignment at the receiver with the acquired CSI. After the MF precoding that leads to the maximal-ratio transmission (MRT), the transmitted signal can be expressed as

$$s(t) = \begin{cases} A\frac{h^*}{|h|}\cos(2\pi f_c t + \theta) & \text{for } s_s(t), \\ \sqrt{\frac{2P_T}{N}}\frac{h^*}{|h|}\sum_{n=1}^{N}\cos[2\pi f_{(n)}t] & \text{for } s_m(t). \end{cases} \tag{3.23}$$

Receiver Architecture. A new receiver architecture is shown in Figure 3.5, which consists of three (energy/information/PAPR) paths and an adaptive PM-&-ID module. To enable the receiver to perform both ID and EH from the same signal, the power splitting is performed in front of the three paths with power-splitting ratio ρ ($0 \leq \rho \leq 1$). We assume that infinitesimally small ρ is enough for reliable ID with the integrated receiver [12]. Then, the received signal in the *energy path* can be expressed as

$$y_{EH}(t) = \sqrt{1 - \rho}hs(t) + \eta(t), \tag{3.24}$$

where $\eta(t) \sim \mathcal{N}(0, \sigma^2)$. The resulting DC power P_{EH} is evaluated as

$$P_{EH} = \zeta_{NL}(N, P_{in}) \times P_{in}, \tag{3.25}$$

where ζ_{NL} is a nonlinear PCE function given N and $P_{in} = \mathbf{E}\{|y_{EH}(t)|^2\} = (1 - \rho)|h|^2 P_T = (1 - \rho)P_R \cong P_R$ (noise energy ignored), which is used for charging the battery and ID in the information path (see Figure 3.5). As the signal power in the energy path is sufficiently large to ignore the noise, the energy-level ID can be performed reliably with high SNR, unlike conventional SWIPT.

The received signal in the *information path* is of the form

$$y_{ID}(t) = \sqrt{\rho}hs(t) + \eta(t), \tag{3.26}$$

which is used to decode the phase information for a given energy level. Since channel estimation is required, decoding in the information path causes more circuit power consumption than PAPR based decoding. Note that the energy and information paths are jointly combined here for single tone SWIPT.

The *PAPR path* is used for PAPR based ID. For this, a PAPR estimator measures the PAPR of the received signal envelope by dividing the peak power with the root mean square (RMS) power. The received PAPR in FF channel is evaluated as

$$PAPR = \frac{\max_{t \in [0,T_m]}|y_{ID}(t)|^2}{\frac{1}{T_m}\int_{T_m}|y_{ID}(t)|^2 dt} \cong 2N. \tag{3.27}$$

PAPR based ID does not require power-hungry active devices, such as mixer and ADC, as well as channel estimation. Furthermore, the efficiency of WPT is enhanced in the low power region, and the PAPR path is suitable for low circuit power consumption while increasing the operational range with lower rate.

Adaptive Mode Switching. In conventional SWIPT, the achievable rate depends on the distance from the AP. With the proposed dual mode operation for SWIPT, however, the rate dependence can be mitigated well, leading to an increased operational range. The achievable rates with single and multi-tone modes are evaluated as

$$R_s = [1 - p_{out}(M)]\log_2 M, \tag{3.28}$$

$$R_m = \frac{1}{B_c T_m}[1 - p_{out}(Q)]\log_2 Q, \tag{3.29}$$

respectively, where $B_c = T_s^{-1}$. The outage probability can be defined as $p_{out} = \Pr[p_b > p_{tag}]$, i.e. the BER given M or Q is higher than the target BER p_{tag}. We assume that $p_{tag,s}$ for the single tone mode is lower than $p_{tag,m}$ for the multi-tone mode because the former requires tight QoS for high data rate. Also, the circuit power consumption should not exceed the harvested power to ensure the energy causality at the receiver. Note that the energy constraint of each mode is different because the single tone mode requires a more complex decoding procedure due to the channel estimation than the multi-tone mode with PAPR based ID.

We can formulate an adaptive MS optimization problem which chooses a proper mode with modulation index M and multi-tone Q to maximize the achievable rate, depending on the received power threshold P_{th} obtained from the nonlinear EH model and the QoS constraints given above. The optimization problem can be formulated as

$$(\text{P1}) : \max_{L} \quad R_x$$
$$\text{s.t.} \quad P_{EH} \geq P_{C,x}, \quad p_b(L) \leq p_{tag,x},$$

where $x \in \{s, m\}$, $L \in \{M, Q\}$, $P_{C,s}$ ($P_{C,m}$) is the circuit power consumption of the single tone (multi-tone) mode. We can obtain the optimal solution (M^*, Q^*) numerically by running the algorithm described below. Note that, if M^* or Q^* is less than 2, the transceiver is assumed to operate for EH only.

Algorithm 1   Algorithm for adaptive MS policy

Initialize M,Q and calculate P_{EH} from P_{in}
if $P_{in} \geq P_{th}$ and $P_{EH} \geq P_{C,s}$ **then**
  Choose maximum M such that BER constraints are met
  return M^*
else if $P_{in} < P_{th}$ and $P_{EH} = P_{C,m}$ **then**
  Choose minimum Q such that BER constraints are met
  return Q^*
else
  return $M^* = 1$ and $Q^* = 1$
end if

Evaluation. The performance of dual mode SWIPT and conventional SWIPT is compared. We assume $P_T = 40$ dBm and $B_c = 1$ MHz where f_c is 900 MHz. We consider a Rayleigh FF channel with path-loss exponent 2.5. Also, the noise power is assumed to be -130 dBm/Hz and ρ is set to 10^{-6}. Here, we have assumed that the single tone mode needs a strict BER constraint to support high data rates. Thus, the target BER of each mode is set to $p_{tag,s} = 0.01$ and $p_{tag,m} = 0.05$, accordingly. We set $P_{th} = 0.5$ mW, and the energy causality constraint is set to be $P_{C,s} = 0.2$ mW and $P_{C,m} = 0.01$ mW.

Figure 3.6 shows the achievable rate versus the distance from the AP subject to the QoS constraints. The rate is obtained by taking the average over different channel realizations. Compared to conventional SWIPT, dual mode SWIPT increases the operational range, where MS occurs at around 5 m for the given P_{th}. We see that dual mode SWIPT provides not only an increased operational range compared to conventional SWIPT with quadrature amplitude modulation (QAM), but also yields higher achievable rate than the multi-tone (PAPR) SWIPT when the receiver is close to the transmitter. This is because the adaptive MS policy allows the choice of optimum values for M and Q according to the received power for maximum rate.

3.4 Energy Harvesting Circuit Design

The nonlinear rectification process also characterizes the saturation effects where the efficiency of WPT rapidly decreases as the RF input power exceeds a certain threshold. To overcome this saturation nonlinearity, we propose a reconfigurable energy harvester to split the RF input power of the rectifier
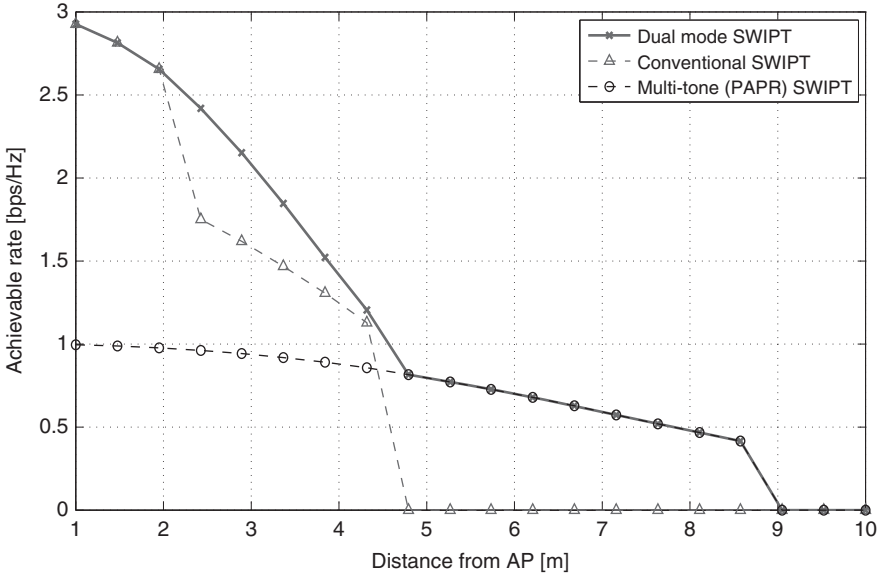
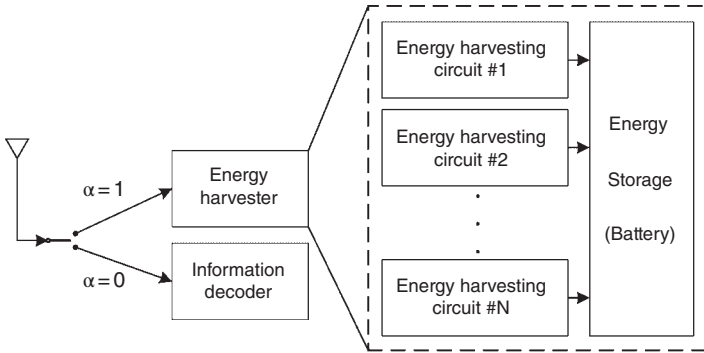**Figure 3.6** Achievable rate distribution subject to the QoS constraints.

Figure 3.7 The proposed receiver structure for SWIPT.

among multiple EH circuits to ensure its reliable operation outside the saturation region.

Proposed Reconfigurable Energy Harvester. Figure 3.7 shows the proposed receiver structure with N_{EH} multiple EH circuits implemented in parallel and followed by a battery. The nonlinear energy harvester is reconfigured adaptively depending on the received power. We assume an identical nonlinear EH model for each EH circuit. Hence, the harvested power at the ith EH circuit, denoted by $P_{EH,i}$, is expressed as

$$P_{EH,i}(\alpha, P_R) = \alpha \; \frac{P_{sat}(1 - e^{-c_1 P_R})}{1 + e^{-c_1(P_R - c_0)}}. \tag{3.30}$$

Here, the mode switching indicator variable α is set to either ID ($\alpha = 0$) or EH ($\alpha = 1$), considering the channel state, as shown in Figure 3.7.

When $\alpha = 1$, all received signal is fed to the energy harvester and then split evenly among N_{EH} multiple EH circuits. We assume an ideal energy harvester such that there is no energy loss during power splitting and energy conversion from multiple EH circuits to the battery. Under the ideal EH assumption, the harvested power at the battery is linearly increased to

$$P_{EH,tot} = \sum_{i=1}^{N_{EH}} P_{EH,i}(\rho_i P_R), \tag{3.31}$$

where ρ_i is the power-splitting ratio for the ith EH circuit. As each EH circuit is modeled by the identical nonlinear function with $\rho_i = 1/N_{EH}$ and $P_{EH,i} = P_{EH,1}$ for $\forall i$, the total harvested power becomes

$$P_{EH,tot} = N_{EH} P_{EH,1}(P_R/N_{EH}). \tag{3.32}$$

To gain some insights into the effect of the power-splitting ratio $\boldsymbol{\rho} = [\rho_1, ..., \rho_{N_{EH}}]$, we consider a toy example of the energy harvester with two EH circuits in parallel. In this case, we can drop the circuit index of the power-splitting ratio and simplify the total harvested power to

$$P_{EH,tot}(\rho, P_R) = P_{EH,1}(\rho P_R) + P_{EH,1}((1 - \rho)P_R), \tag{3.33}$$

where $\rho \in [0, 1]$. $P_{EH,tot}$ varies as the power-splitting ratio ρ or the received power P_R changes. With fixed P_R, $P_{EH,tot}$ can be maximized by optimizing ρ.

Figure 3.8 illustrates $P_{EH,tot}$ as a function of ρ and P_R while Figure 3.9 shows the contours of $P_{EH,tot}$ as functions of ρ and P_R. The parameters of the practical EH circuits here are set to $P_{sat} = 3mW$, $c_0 = 0.0033$, and $c_1 = 1000$. We observe that the optimal power-splitting ratio ρ^* changes with the received power P_R. When P_R is low, only one EH circuit is activated while switching off the other by setting $\rho = 0$ or 1. For high P_R, it is preferable to activate both EH circuits by splitting the received power evenly ($\rho = 0.5$). This is a direct consequence of the nonlinear behavior of the EH circuit. The EH efficiency becomes very low for low P_R, and thus using a single EH circuit is better than using both. On the other hand, using a single EH circuit causes saturation for high P_R, and it is desirable to activate both EH circuits. When saturation occurs, splitting the received power evenly can reduce the excess power due to the saturation. Based on these observations from the above toy example, the total harvested power can be expressed as $P_{EH,tot} = \max\{P_{EH,1}(P_R), \; 2P_{EH,1}(P_R/2)\}$.

When the number of EH circuits increases, we can reconfigure the energy harvester in a similar manner according to the received power with even split. The total harvested power is $P_{EH,tot} = \hat{N}_{EH} P_{EH,1}(P_R/\hat{N}_{EH})$, where $\hat{N}_{EH}$ is the
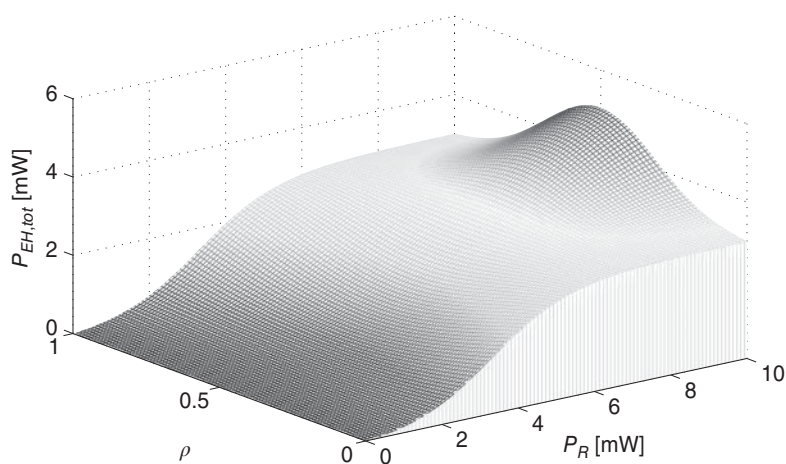
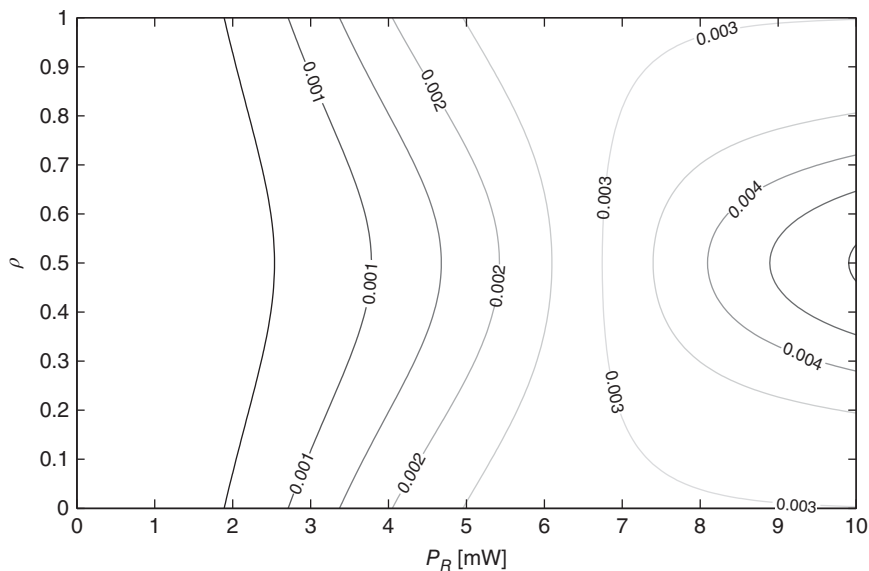**Figure 3.8** The harvested power depending on the received power P_R and ρ.

Figure 3.9 Contour of the harvested power versus the received power P_R.
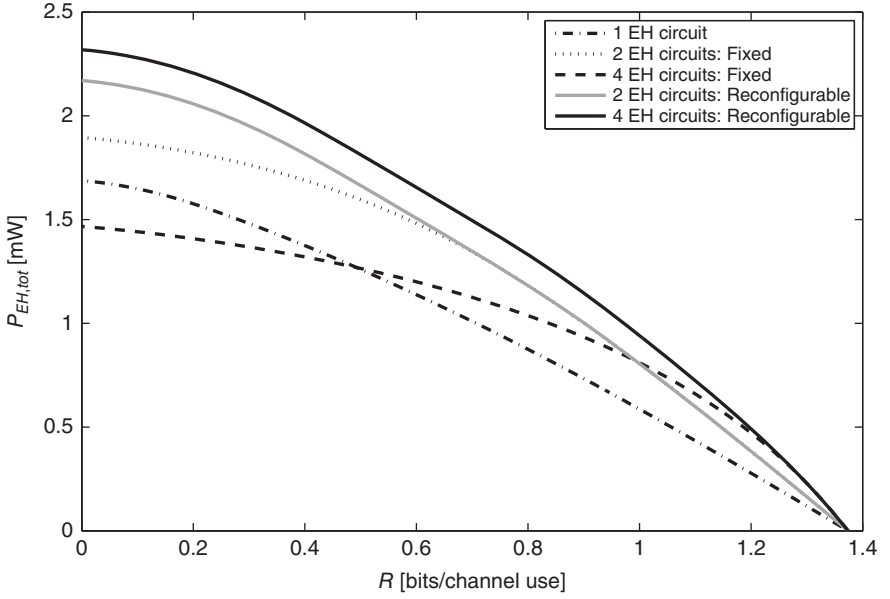
Figure 3.10 The rate–energy tradeoff.

number of activated EH circuits depending on the received power. $\hat{N}_{EH}$ can be determined by $\hat{N}_{EH} = \arg\max_{N_{EH}} \{P_{EH,1}(P_R), ..., N_{EH}P_{EH,1}(P_R/N_{EH})\}$, yielding the optimal power-splitting ratio $\rho_i^* = 1/\hat{N}_{EH}, i \in \{1, ..., \hat{N}_{EH}\}$.

Evaluation. To validate the performance improvements by the reconfigurable energy harvester, we evaluate the rate–energy tradeoff as

$$C_{R-E} = \bigcup_\alpha \{(R, P_{EH}) : R \leq \mathbf{E}\{R(\alpha)\}, P_{EH} \leq \mathbf{E}\{P_{EH,tot}(\alpha, \boldsymbol{\rho}^*)\}\} \qquad (3.34)$$

where $R(\alpha) = (1 - \alpha)\log_2(1 + P_R/\sigma^2)$. The parameters for each EH circuit are set to $P_{sat} = 3mW$, $c_0 = 0.0033$, and $c_1 = 1000$. In the simulation, we have used $B = 10^5$ fading blocks, each of which was generated from the Rician fading channel. We assume that the power gain of the LOS channel is -30 dB with Rician factor 1. The noise variance is set to yield an average SNR of 3 dB, regardless of the received power, to ensure a fair comparison.

Figure 3.10 shows the rate–energy tradeoff when the transmit power is 5 W. We first compare the receiver with fixed multiple EH circuits ($N_{EH} = 2, 4$) with that with a single EH circuit ($N_{EH} = 1$). We see that using two EH circuits yields more harvested energy compared to using a single or four EH circuits. If the reconfigurable receiver ($N_{EH} = 2, 4$) is used, using more circuits always yields better performance. Thus, the reconfigurable receiver always has better performance than the receiver with fixed multiple EH circuits. Their harvested power

gap decreases as the rate increases. Consequently, the former has much better performance when the rate is low or the energy constraint is tight, suitable for low-power smart devices that are self-powering.

3.5 Discussion and Conclusion

First, we implemented multi-tone SWIPT using PAPR based signaling and a combined receiver that realizes the RF-to-DC conversion at once, both for ID and EH, with no channel estimation. In particular, the PAPR based ID over a selective sub-band offers a *reliable* BER performance regardless of the specific channel gain, as long as the sub-band has an FF channel. Using multi-tone waveforms was shown to be the prerequisite for efficient WPT, and in conjunction with PAPR based ID it leads to a promising solution for realizing low-power smart devices, eventually with batteryless operation, facilitating the massive and dense deployment of MTC for IoT.

Second, we have designed a dual mode SWIPT transceiver alternating between single and multi-tone waveforms. We also developed the new concept of adaptive MS based on the nonlinear EH model. The dual mode operation mitigates the energy causality constraint and increases the operational range. It was demonstrated that dual mode SWIPT provides significant gains in achievable rate distribution over the conventional one. In particular, the adaptive MS algorithm was shown to be a viable solution for enlarging the operational range, leading to self-powering for energy neutral operation.

Third, we have proposed a reconfigurable energy harvester with multiple EH circuits implemented in parallel before the battery. We showed how the practical energy harvester can be reconfigured based on the received power. To verify the performance improvement, we have investigated the rate–energy tradeoff. The reconfigurable receiver was compared with two other receivers: one with a single EH circuit and the other with fixed multiple EH circuits. The performance evaluations showed that the reconfigurable receiver achieves the best rate–energy tradeoff, with which SWIPT can self-power smart devices effectively while ensuring energy neutral operation.

Bibliography

1 X. Lu, P. Wang, D. Niyato, D.I. Kim, and Z. Han (2015) Wireless networks with RF energy harvesting: A contemporary survey. *IEEE Commun. Surveys & Tutorials*, **17** (2): 757–789.

2 X. Lu, P. Wang, D. Niyato, D.I. Kim, and Z. Han (2016) Wireless charging technologies: Fundamentals, standards, and network applications. *IEEE Commun. Surveys & Tutorials*, **18** (2): 1413–1452.

3 V. Liu, A. Parks, V. Talla, S. Gollakota, D. Wetherall, and J.R. Smith (2013) Ambient backscatter: Wireless communication out of thin air. *ACM SIGCOMM 2013*, Hong Kong, China, pp. 39–50.

4 V. Talla, M. Hessar, B. Kellogg, A. Najafi, J.R. Smith, and S. Gollakota (2017) LoRa backscatter: Enabling the vision of ubiquitous connectivity. *ACM UBICOMM 2017*, **1** (3): 105:1–105:24.

5 R. Eletreby, D. Zhang, S. Kumar, and O. Yagan (2017) Empowering low-power wide area networks in urban settings. *ACM SIGCOMM 2017*, Los Angeles, CA, pp. 309–321.

6 S. Bi, C.K. Ho, and R. Zhang (2015) Wireless powered communication: Opportunities and challenges. *IEEE Commun. Mag.*, **53** (4): 117–125.

7 K. Huang and X. Zhou (2015) Cutting the last wires for mobile communications by microwave power transfer. *IEEE Commun. Mag.*, **53** (6): 86–93.

8 A.S. Boaventura and N.B. Carvalho (2011) Maximizing DC power in energy harvesting circuits using multisine excitation. *2011 IEEE MTT-S International Microwave Symposium Digest (MTT)*, Baltimore, MD, pp. 1–4.

9 B. Clerckx and E. Bayguzina (2016) Waveform design for wireless power transfer. *IEEE Trans. Signal Process.*, **64** (23): 6313–6328.

10 D.I. Kim, J.H. Moon, and J.J. Park (2016) New SWIPT using PAPR: How it works. *IEEE Wireless Commun. Lett.*, **5** (6): 672–675.

11 R. Zhang and C.K. Ho (2013) MIMO broadcasting for simultaneous wireless information and power transfer. *IEEE Trans. Wireless Commun.*, **12** (5): 1989–2001.

12 X. Zhou, R. Zhang, and C.K. Ho (2013) Wireless information and power transfer: Architecture design and rate–energy tradeoff. *IEEE Trans. Commun.*, **11**: 4754–4767.

13 L. Liu, R. Zhang, and K.C. Chua (2013) Wireless information transfer with opportunistic energy harvesting. *IEEE Trans. Wireless Commun.*, **12** (1): 288–300.

14 E. Boshkovska, D.W.K. Ng, N. Zlatanov, and R. Schober (2015) Practical nonlinear energy harvesting model and resource allocation for SWIPT systems. *IEEE Commun. Lett.*, **19** (12): 2082–2085.